J. Fluid Mech. (2007), *vol.* 589, *pp.* 455–478.
doi:10.1017/S0022112007008130 Printed in the United Kingdom

A dissipative point-vortex model for nearshore circulation

E. TERRILE[1] AND M. BROCCHINI[2]

[1]DICAT, Università di Genova, 16145 Genova, Italy
[2]Istituto di Idraulica e Infrastrutture Viarie, Università Politecnica delle Marche, 60131 Ancona, Italy

(Received 26 July 2006 and in revised form 26 June 2007)

The hydrodynamic circulation of a nearshore region with complex bathymetry is investigated by means of a point-vortex approach similar, but more complete and suited to practical applications, to that of Kennedy (*J. Fluid Mech.* vol. 497, 2003, p. 225). The generation and dissipation of each single-point vortex are analysed in detail to obtain a complete description of the vortex dynamics. In particular, we clarify how the mechanism for the generation of breaking-wave-induced macrovortices (large-scale two-dimensional horizontal vortices) can be practically implemented and we discuss in detail the mechanism leading to the dissipation of the circulation assigned to each vortex. Available approximate relations for the rate of generation of bar vortices are placed in context and discussed in detail, and novel approximate relations for the shore vortex generation and for the vortex viscous dissipation are proposed, the latter largely improving the description of the point vortex dynamics. Results have been obtained using three 'typical' rip-current bathymetries for which we also test qualitatively and quantitatively the model comparing the vorticity dynamics with the results obtained by means of both wave-resolved and wave-averaged circulation models. A comparison of dynamically equivalent flow configurations shows that the dissipative point-vortex model solutions, neglecting any influence of the wave field, provide rip current velocities in good agreement with both types of numerical solution. A more complete description of the rip current system, not limited to the rip-neck region as given by Kennedy (2003) by mean of an inviscid model, has been achieved by including dissipative effects.

1. Introduction

As shown theoretically (Peregrine 1998, 1999; Bühler 2000), differential wave breaking generates circulation and vorticity which re-organizes in macrovortices, large-scale horizontal eddies with vertical axis. Numerical studies on the generation of such breaking-wave-induced macrovortices have been performed on different topographies (Bühler & Jacobson 2001, hereinafter BJ; Brocchini *et al.* 2004). All these studies were focused on the generation of macrovortices and the subsequent vortex evolution. Predictive expressions were derived for the generation of circulation once given the geometry and the incident wave conditions. Vortices generated in the nearshore zone typically migrate because of mutual interaction and self-advection. Both mechanisms are influenced by the bottom slope and, therefore, the vortex dynamics is directly influenced by the bathymetry. In particular, self-advection, which is the contribution to the vortex motion owing to the presence of a sloping bed, forces the vortex to move along isobaths. Such self-advection can be approximately

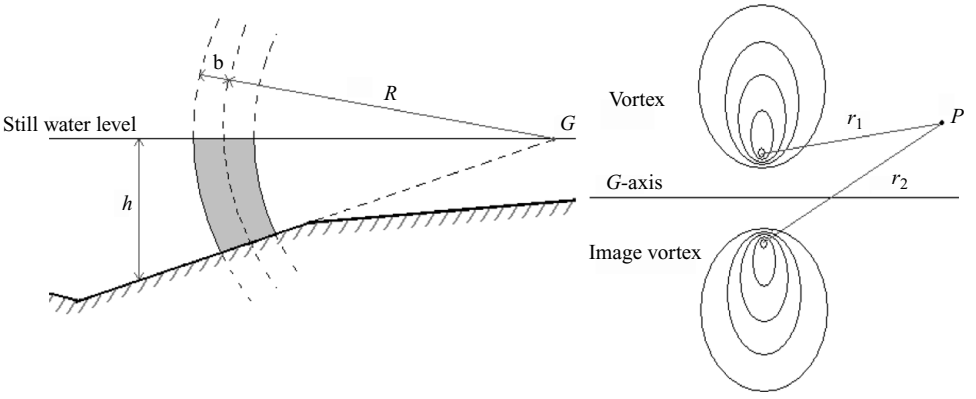

FIGURE 1. (*a*) The virtual extension of the vortex tube to a three-dimensional vortex ring of radius R. (*b*) Streamlines for a vortex and its image, distances r_1 and r_2 to the point P.

modelled by regarding the macrovortices (of core radius b in figure 1) as portions of vortex rings with radius equal to the distance R between each macrovortex and the projection of the slope on the water level, axis G. In the case of a planar sloping beach, this coincides with the shoreline (e.g. BJ).

The generation and transport of start-up macrovortices for topographically controlled breaking waves has been studied by Brocchini *et al.* (2004) and Kennedy *et al.* (2006). Notwithstanding the difficulties in setting up an appropriate laboratory experiment focused on breaking-wave-induced macrovortices, a few laboratory observations are now available (e.g. Haller, Dalrymple & Svendsen 2002; Centurioni 2002; Kennedy & Thomas 2004; Piattella, Brocchini & Mancinelli 2006).

Kennedy (2003) reproduced in a simplified manner, but with fairly good results, the rip-current neck evolution by means of a point-vortex (PV) model. The model is based on a generation-of-vorticity approach, where oppositely signed vortices are continuously released in the most appropriate generation zone and set free in the domain. The model is valid not only for a flat bed, but also for any generic bathymetries, and the vorticity sources are those due to wave breaking. Once the location and the intensity of such vorticity sources are known, the problem becomes that of predicting the resulting vortex dynamics.

A more reliable description of nearshore vortical flows and dynamics must account not only for the adequate knowledge of the rate of generation of the macrovortices, but also for the rate of circulation dissipation to which they are subjected. During their evolution, vortices are mainly dissipated by the 'classical' eddy-viscosity effects (see Terrile *et al.* 2006) and, obviously, by bottom friction (e.g. BJ).

A complete PV model, which describes the main rotational phenomena taking place in the nearshore zone, can both represent a starting point for the realization and validation of more complex circulation models for use in the case of highly vortical flows and provide a simplified but useful insight into specific coastal circulation problems.

With this aim and to promote a 'vorticity approach' for the analysis of the nearshore circulation, we propose a PV model which improves that of Kennedy (2003) in two main ways: (*i*) viscous dissipative mechanisms are included to provide a suitable decay/smoothing of the velocity field; (*ii*) a more realistic topography, inclusive of shore-vortices, is analysed as described in Kennedy *et al.* (2006).

In § 2, we give a description of the processes undergone by vortical flows over a generic topography. A detailed analytical description of the dissipation of a single-point vortex is provided in § 3, whereas in § 4, we examine the processes which lead to the generation of the vortex and circulation by each single breaking wave on a longshore-varying topography. In § 5, the dynamics of the dissipation of a single-point vortex on different topographies is analysed, and the complete flow circulation at a complex bathymetry is described. Discussion and conclusions are given in § 6.

2. Vortex dynamics over a sloping barred beach

The motion of a vortex, over a complex topography can be regarded as forced by two distinct effects: the mutual advection with eventual surrounding vortices and the self-advection due to an uneven topography. The processes of macrovortex transport over a complex topography are described in Brocchini *et al.* (2004) and Kennedy *et al.* (2006).

They have been grouped in four different stages. In the first stage, a general shoreward motion from breaking waves is by far the strongest. During stage 2, mutual-advection and self-advection dominate, being the irrotational portion of breaking-wave forcing in balance with the surface-elevation forcing. In stage 3, the vortices leave the areas of generation, and self-advection becomes less important than mutual-advection. Finally, in the fourth stage, interactions among consecutively generated vortices and circulation dissipation become the main dynamical effects. Stages 4 and 1 are analysed in detail in §§ 3 and 4, respectively, whereas this section sets the scene for the whole model.

Neglecting bottom friction and in the absence of wave breaking, the circulation in shallow waters, defined as $\Gamma \equiv \oint \boldsymbol{v} \cdot \mathbf{d}\boldsymbol{l}$, is conserved along any material circuit, satisfying Kelvin's circulation theorem. According to the classical inviscid theory, in the case of a constant water depth, the resulting velocity field, at a point of an infinite domain, is given by:

$$v_\theta = \frac{\Gamma}{2\pi r}, \tag{2.1}$$

where v_θ is the velocity orthogonal to the radius r, in a right-hand sense, which connects the considered point P with the vortex core. If the circulation Γ is conserved, the azimuthal velocity v_θ around a vortex must decay inversely proportional to r.

Equation (2.1) is valid in the far field, while moving in the region closer the shoreline it loses accuracy. Here, the streamfunction for a single-point vortex is obtained, approximating the vortex as a portion of a three-dimensional 'virtual' vortex ring (Lamb 1932) of radius R (figure 1). The effects of the shoreline are, therefore, taken into account through use of an image vortex as shown in figure 1. The Stokes streamfunction of a point vortex that includes the shoreline effects on a planar beach is given by the following expression (e.g. Kennedy *et al.* 2006):

$$\psi = -\frac{s\Gamma}{2\pi}(r_1 + r_2)\{K(m) - E(m)\} \quad \text{where} \quad m = \left(\frac{r_2 - r_1}{r_2 + r_1}\right)^2. \tag{2.2}$$

Here, s is the slope of the piecewise planar beach, h is assumed to be the local water depth, r_1 and r_2 are the distances between the point considered P and the core of either the vortex or its image (figure 1). $K(m)$ and $E(m)$ are complete elliptic integrals of the first and second kind, in terms of the parameter m. In this case, the depth-averaged velocity field, $\boldsymbol{v} = (v_x, v_y) = (u, v)$, can be obtained through the definition of

a streamfunction ψ such that:

$$u = -\frac{1}{h}\frac{\partial \psi}{\partial y}, \quad v = \frac{1}{h}\frac{\partial \psi}{\partial x}, \tag{2.3a,b}$$

are, respectively, the onshore and longshore velocity components. This derives from the assumption of neglecting water surface oscillations to study the vortex dynamics (this means using a rigid upper lid approximation at $d = h + \eta$, where d is the total water depth and η is the free-surface elevation).

From (2.2)–(2.3), the velocity field induced by a vortex pair/couple at a generic point P is easily computed, by just knowing the distances r_1 and r_2. In particular, the mutual-advection between two vortices is obtained assuming the distances between one vortex core and the core of both the other vortex and its image. Obviously, the mutual-advection velocity component induced on each vortex is the sum of all contributions given by the others vortices in the domain. To obtain the total velocity to which each vortex is subjected, we must add the self-advection contribution. Such self-advection is approximated by the self-advection of a three-dimensional vortex ring with radius R (see figure 1). Assuming R to be locally proportional to the water depth h, we can obtain a simple approximation of the flow induced by the local slope. The radius is, therefore, assumed as $R = h/|\nabla h|$.

Following Lamb's (1932) approach, the approximate vortex velocity of propagation in an inviscid fluid is:

$$\frac{\Gamma}{4\pi R}\left\{\ln\left(\frac{8R}{b}\right) - \frac{1}{4}\right\}, \tag{2.4}$$

where b is the core radius, which should be much smaller than R.

According to the inviscid theory, the vorticity is assumed to be uniformly distributed over the cross-section of the vortex. From (2.4), it is clear that by increasing the core radius b, the self-advection velocity decreases.

It is obvious that near the centre of the vortex the velocity and its radial gradient become so large that it is necessary to include some dissipative effects to obtain a more appropriate description of the flow. Viscous damping is then taken into account, approaching the centre of the vortex, through the 'boundary-layer technique' (e.g. Tung & Ting 1967; Saffman 1970). The solution of the inner viscous core is given as a power series of the small parameter ϵ (defined in the following) and matched with the solution of the outer inviscid region. The typical length scale for the outer region can be taken as the vortex ring radius R, while for the inner region it should be of the order of $(\nu t)^{1/2}$, ν being the kinematic viscosity. However, because of the turbulent nature of the phenomena we describe, we consider it more appropriate to use a local eddy viscosity ν_T, which is here taken as constant inside each single-core vortex. Therefore, Γ and R being the only physical quantities associated with the vortex, the appropriate time scale is R^2/Γ and the length scale for the inner region is taken as $R(\nu_T/\Gamma)^{1/2}$. Hence, the expansion parameter ϵ is taken as the ratio between those two typical length scales (inner/outer):

$$\epsilon = \left(\frac{\nu_T}{\Gamma}\right)^{1/2}. \tag{2.5}$$

Note that the reference Reynolds number is $Re_\Gamma = |\Gamma|/\nu_T$, hence $\epsilon = (Re_\Gamma)^{-1/2}$.

Viscosity acts to diffuse vorticity and it influences the self-advection velocity. The speed of propagation of a thin vortex ring, assuming the vorticity concentrated as a 'δ-function', at a fixed time t_{in}, was derived by Tung & Ting (1967) and, at the zeroth

order, which is the one used in our simplified model, is approximated as:

$$\frac{\Gamma}{4\pi R}\left\{\ln\left(\frac{8R}{2\sqrt{\nu_T\tau}}\right)-0.688\right\}. \tag{2.6}$$

The time variable τ used in (2.6), measured from the instant t_{in} when the vortex is introduced in the domain, is defined as:

$$\tau(t)=\frac{\displaystyle\int_{t_{in}}^{t} R(t')\,\mathrm{d}t'}{R(t)}, \tag{2.7}$$

where the time dependence of the ring radius $R(t)$ is caused by the vortex moving over different water depths h and slopes $|\nabla h|$. (Note that for $\nabla h=0$, i.e. for $R\to\infty$, (2.7) is still well-behaved, but the 'vortex-ring approximation' fails.)

The radius of the ring for the leading term of the inner solution can be considered infinite (i.e. Tung & Ting 1967), therefore, the inner core of the vortex can be described approximately as the same as that of an infinite straight vortex line, whose decay solution can be found in Lamb (1932). This means that the local distribution found at the leading order which, apart from use of the time variable τ instead of t, corresponds to the Lamb–Oseen diffusing vortex, is used to obtain (2.6). Inside the vortex core, viscosity acts to diffuse vorticity owing to an initial strength Γ concentred in the vortex centre. Such a diffusive effect leads to the following azimuthal velocity and vorticity valid inside the vortex core and given, respectively, by:

$$v_\theta=\frac{\Gamma}{2\pi r}[1-\exp(-r^2/(4\nu_T\tau))],\quad \hat{\omega}=\frac{\Gamma}{8\pi\nu_T t}\exp(-r^2/(4\nu_T\tau)). \tag{2.8a,b}$$

Moving with a single vortex, the ring radius changes in time as a function of the local bathymetry, hence, following Tung & Ting (1967), the core vortex radius in a first approximation, can be taken as:

$$b=2(\nu_T\tau)^{1/2}. \tag{2.9}$$

Hence, the vortex self-advection velocity $\boldsymbol{v}_{sa}$ can be written by manipulating (2.6) to obtain an expression in which the dependence of the velocity on h is easily seen:

$$\boldsymbol{v}_{sa}=\frac{\Gamma}{4\pi}\frac{\nabla h}{h}\times\hat{\boldsymbol{k}}\ \mathscr{A}(x,y,t), \tag{2.10}$$

and where $\hat{\boldsymbol{k}}$ is the unit vector in the z-direction and pointing upward and the function $\mathscr{A}$ is defined as:

$$\mathscr{A}(x,y,t)=\ln\left(\frac{4}{\sqrt{\nu_T\tau}}\frac{h}{|\nabla h|}\right)-0.688. \tag{2.11}$$

Note that during the vortex motion the only parameter which varies is h. Γ_{in} is the initial circulation intensity (introduced in the domain with the vortex). Self-advection velocities in the x- and y-directions, are, respectively:

$$u_{sa}=\frac{\Gamma_{in}}{4\pi}\frac{h_{,y}}{h}\mathscr{A}(x,y,t),\quad v_{sa}=\frac{-\Gamma_{in}}{4\pi}\frac{h_{,x}}{h}\mathscr{A}(x,y,t). \tag{2.12}$$

Once mutual-advection and self-advection velocities of the vortices are known, it becomes important to quantify the rate of generation (through Γ) and dissipation (through ν_T) of the vortices.

In particular, inhomogeneities in the alongshore direction, typical of real surf zone flows, can arise because of either the topography or the incident waves. Of course,

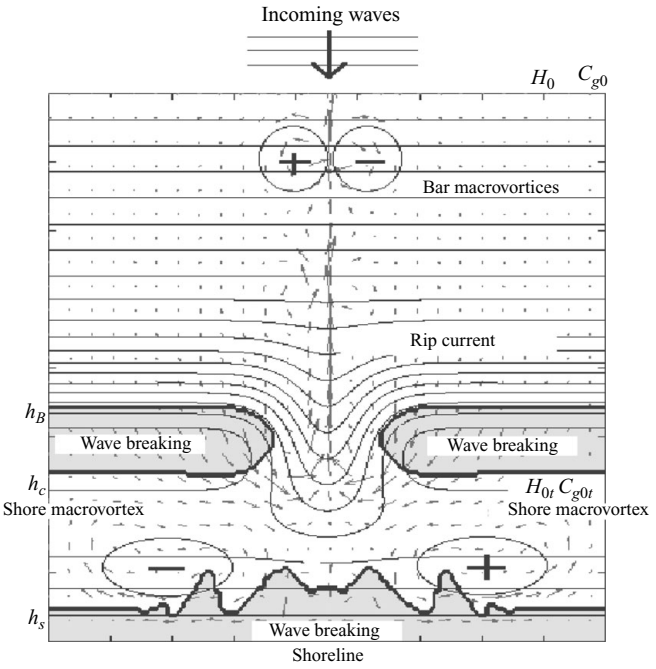

FIGURE 2. Example of the circulation pattern in a nearshore area with complex topography and with 'typical' bar vortices and shore vortices. The grey areas indicate the regions of wave breaking as derived from wave-averaging sample computations described in § 5. Flow variables used in the analytical modelling of vorticity generation detailed in § 4 are also shown.

an inhomogeneous topography would generate inhomogeneity of the waves, but also a spatially non-uniform wavetrain approaching the beach, is characterized by differential breaking and generates strong mean-flow vorticity.

The circulation forcing depends only on the details of wave breaking on the bar, not on bar length or rip channel width. Peregrine's (1998) results are for bore theory, where breaking locations and integrals of evolution in space can be difficult to estimate.

The mean rate of generation of circulation ($\mathrm{D}\Gamma/\mathrm{D}t$) is due to differential breaking along a wave ray, and the order of magnitude of the core radius of each vortex can be considered proportional to the wave energy gradient along the same wave ray. As illustrated by Kennedy *et al.* (2006), in the case of a barred beach, two types of vortices are generated, the bar vortices and the shore vortices. In figure 2, a sketch of the typical nearshore circulation is given and the locations, where the bar vortices and the shore vortices are generated, are shown. Since each wave can, potentially, generate a single-point vortex, the upper limit for the core radius must be the wavelength L.

3. The dissipation of the point-vortices circulation

A PV model is naturally built within a Lagrangian framework, the most suited to describing the dynamics when following each vortex. Hence, the dissipation and the generation of the circulation Γ for the point vortices are here studied using such an approach (e.g. BJ).

We here analyse in detail the dissipation of a single-point vortex generated at a given location of water depth h_{in}, with core radius b_{in} and intensity Γ_{in} and moving over a generic topography.

We first derive the circulation equation in the nonlinear shallow-water-equation (NSWE) framework taken as the most suited for the flow at hand. The continuity and momentum equations of the classical NSWE are reported below, making use of the rigid-lid approximation:

$$(uh)_{,x} + (vh)_{,y} = 0, \tag{3.1}$$

$$u_{,t} + uu_{,x} + vu_{,y} + \left(\frac{p}{\rho}\right)_{,x} = F_x - B_x, \tag{3.2}$$

$$v_{,t} + uv_{,x} + vv_{,y} + \left(\frac{p}{\rho}\right)_{,y} = F_y - B_y, \tag{3.3}$$

in which $(\,)_{,x}$ and $(\,)_{,y}$ give partial differentiation with respect to x and y, $h = h(x, y)$ is the local water depth, $p = p(x, y, t)$ is the pressure at the rigid lid, ρ is the (constant) water density, $\boldsymbol{B} = (B_x, B_y, 0)$ is the vector of the bottom friction and $\boldsymbol{F} = (F_x, F_y, 0)$ is the vector of the dissipative body forces. The latter is expressed in terms of the depth-averaged effective stress tensor $\boldsymbol{T}$ of components T_{xx}, $T_{xy} = T_{yx}$, T_{yy} (e.g. Brocchini & Colombini 2004):

$$F_x = \frac{(hT_{xx})_{,x} + (hT_{xy})_{,y}}{h}, \quad F_y = \frac{(hT_{xy})_{,x} + (hT_{yy})_{,y}}{h}. \tag{3.4a,b}$$

Usually, simple closures are considered for both the bottom friction,

$$B_x = \frac{c_f|\boldsymbol{v}|u}{h}, \quad B_y = \frac{c_f|\boldsymbol{v}|v}{h}, \tag{3.5a,b}$$

and the effective stresses,

$$T_{xx} = 2\nu_T u_{,x}, \quad T_{xy} = T_{yx} = \nu_T(u_{,y} + v_{,x}), \quad T_{yy} = 2\nu_T v_{,y}, \tag{3.6a–c}$$

in which $\nu_T = \nu_T(x, y, t)$ is a depth-averaged eddy viscosity and c_f is a dimensionless friction coefficient which depends on the bottom roughness and is, usually, taken as a constant of order 0.01. In (3.6), not only are turbulent stresses accounted for, but also viscous and dispersive contributions, the latter induced by vertical flow gradients.

The circulation equation can, now, be obtained by integrating the momentum (3.2)–(3.3) equations over a closed material curve. The main aim is to find a suitable equation giving the dissipation rate for the circulation around a closed curve C circling the vortex as a function of the initial condition (Γ_{in}, b_{in} and h_{in}), for which the vortices have been generated, of the local water depth h and of time. The Lagrangian rate of change of Γ can be written as:

$$\frac{\mathrm{D}\Gamma}{\mathrm{D}t} = \frac{\mathrm{D}}{\mathrm{D}t}\oint_C \boldsymbol{v}\cdot\mathrm{d}\boldsymbol{x} = \oint_C \frac{\mathrm{D}v_k}{\mathrm{D}t}\mathrm{d}x_k + \oint_C v_k\frac{\mathrm{D}(\mathrm{d}x_k)}{\mathrm{D}t} \quad \text{where} \quad \frac{\mathrm{D}(\mathrm{d}x_k)}{\mathrm{D}t} = v_{k,j}\mathrm{d}x_j, \tag{3.7}$$

in which k and $j = 1, 2$.

The momentum NSWE (3.2) and (3.3) can be written for the generic kth component as:

$$\frac{\mathrm{D}v_k}{\mathrm{D}t} + \left(\frac{p}{\rho}\right)_{,k} = F_k - B_k. \tag{3.8}$$

Substituting (3.8) into (3.7), we obtain:

$$\frac{\mathrm{D}\Gamma}{\mathrm{D}t} = \oint_C F_k \mathrm{d}x_k - \oint_C B_k \mathrm{d}x_k - \oint_C \left(\frac{p}{\rho}\right)_{,k} \mathrm{d}x_k + \oint_C v_k v_{k,j} \mathrm{d}x_j. \tag{3.9}$$

Applying the Stokes' theorem, (3.9) becomes:

$$\frac{\mathrm{D}\Gamma}{\mathrm{D}t} = \iint_S (\nabla \times \boldsymbol{F}) \cdot \hat{\boldsymbol{k}} \, \mathrm{d}S - \iint_S (\nabla \times \boldsymbol{B}) \cdot \hat{\boldsymbol{k}} \, \mathrm{d}S, \tag{3.10}$$

where S is a surface centred on the point vortex and bounded by C.

Both terms on the right-hand side of (3.10) are analysed in the following. The first can be written, with use of (4.3), in the explicit form:

$$\iint_S (\nabla \times \boldsymbol{F}) \cdot \hat{\boldsymbol{k}} \, \mathrm{d}S = \iint_S \left(\nabla \times \left[\frac{1}{h} \nabla \cdot (h \nu_T \boldsymbol{T})\right]\right) \cdot \hat{\boldsymbol{k}} \, \mathrm{d}S, \tag{3.11}$$

where $\boldsymbol{T}$ is the same as defined by Brocchini & Colombini (2004):

$$\boldsymbol{T} \equiv \begin{pmatrix} 2u_{,x} & u_{,y} + v_{,x} & 0 \\ u_{,y} + v_{,x} & 2v_{,y} & 0 \\ 0 & 0 & 0 \end{pmatrix} = 2\nabla \boldsymbol{u} - \boldsymbol{\Omega}. \tag{3.12}$$

The curl on the right-hand side of (3.11) can be expanded in the same way as in Brocchini & Colombini (2004). An accurate analysis on the generation/dissipation terms in the vorticity and enstrophy equations for coastal models (both wave-averaged and wave-resolving) showed that two 'negative-definite' (always negative) terms arise from the curl of $\boldsymbol{F}$ (see Terrile *et al.* 2006). They describe both the classical viscous effect and the dissipation effect due to the depth gradient '∇h'. A simple comparison shows that the most intense dissipation mechanism, apart from the bottom friction, is due to the classic viscous term, $-\nu_T(\nabla\omega)^2$, while depth gradients weakly contribute. For this reason, in the following, the analysis of the term in (3.11) is simplified by retaining only such viscous terms:

$$\iint_S \left(\nabla \times \left[\frac{1}{h} \nabla \cdot (h \nu_T \boldsymbol{T})\right]\right) \cdot \hat{\boldsymbol{k}} \, \mathrm{d}S \simeq - \iint_S \nu_T (\nabla\hat{\omega})^2 / \hat{\omega} \, \mathrm{d}S, \tag{3.13}$$

where $\hat{\omega}$ is the vorticity, inside the core vortex, given by (2.8*b*).

Of the second term on the right-hand side of (3.10) we only retain the 'negative-definite' contribution for the enstrophy (see Brocchini & Colombini 2004), where 'negative-definite' is used to indicate terms that, in the enstrophy equation, are always negative and, therefore, represent a pure enstrophy dissipation. (In the spirit of PV modelling, no account is, obviously, given of vorticity generation/dissipation which occurs outside the point vortices, e.g. nonlinear bottom friction terms. More details on the overall importance of non-local effects can be found in BJ.) Using (3.5), such terms can be written as follows:

$$-\iint_S \left(\nabla \times \left[c_f \frac{|\boldsymbol{v}|\boldsymbol{v}}{h}\right]\right) \cdot \hat{\boldsymbol{k}} \, \mathrm{d}S \simeq - \iint_S \frac{c_f}{h} |\boldsymbol{v}| \omega \, \mathrm{d}S. \tag{3.14}$$

From (2.8*b*), we can easily evaluate the integral terms of (3.13) and (3.14).

Note that an apparent contradiction can be found between the dissipative viscous models appearing in (2.8) and in (3.13). Differences are reconciled in view of the different spatial scales at which the two viscous models are used. Focusing our attention on the circulation of each single vortex we evaluate (3.13) and (3.14) by

using the vorticity distribution found for each vortex and given by (2.8). In the latter, viscosity contributes to smoothing in time the vorticity $\hat{\omega}$ inside the vortex core and, according to (2.9), to varying the vortex radius. Hence, the viscous mechanism is a local one. On the other hand, use of (3.13), valid over the whole spatial domain, allows us to determine the time decay of the circulation Γ owing to the dissipative terms (3.13) and (3.14).

Expressions of (3.13) and (3.14) have to be evaluated for each vortex while following its motion, i.e. in a Lagrangian manner. Considering a generic point in the domain, the velocity field is mainly due to the mutual-advection velocities generated by all vortices in the neighbourhood. The circulation dissipation found at such generic point depends only on the intensities of all the surrounding vortices, we call such dissipation D_{ma}. If a single vortex is placed at the spatial location, a new contribution should be added: the self-advection velocity due to the new vortex. This gives rise to a further contribution D_{sa} (see (2.8)) to the dissipation of Γ. Hence, the total dissipation is $D_{ma} + D_{sa}$. For this reason we must know the self-rate of dissipation of each vortex with the purpose of studying their own dynamics.

It is now useful, using the vorticity distribution given by (2.8*b*), to evaluate both (3.13) and (3.14), hence allowing for an explicit expression of the dissipation due to viscous and bottom friction effects, respectively. The expressions we obtain, because of the Lagrangian approach, describe the time evolution of the circulation Γ. In particular, in the viscous contribution, because of the axisymmetric distribution of vorticity, $(\nabla\hat{\omega})^2$ is given by:

$$(\nabla\hat{\omega})^2 = \frac{\Gamma^2}{256\pi^2\nu_T^4\tau^4} r^2 \exp(-r^2/(4\nu_T\tau)). \tag{3.15}$$

Since Γ is the intensity of the circulation for each point vortex and, because of the dissipation we are computing while following the vortex, Γ changes in time. From (2.8*b*) and (3.15), we obtain the following term which appears in (3.13):

$$\frac{(\nabla\hat{\omega})^2}{\hat{\omega}} = \frac{\Gamma}{32\pi\nu_T^3\tau^3} r^2 \exp(-r^2/(4\nu_T\tau)). \tag{3.16}$$

This term always assumes the same sign of Γ and, because of the minus sign in (3.13), it always represents a sink for the circulation dynamics of each vortex.

By means of (2.8*a*) and (2.8*b*) and using cylindrical coordinates, for which $\mathrm{d}S = r\,\mathrm{d}r\,\mathrm{d}\theta$ and the axisymmetry condition, (3.13) and (3.14) become, respectively:

$$\iint_S -\nu_T \frac{(\nabla\omega)^2}{\omega}\mathrm{d}S = \int_0^b -\frac{\Gamma}{16\nu_T^2\tau^3} r^3 \exp(-r^2/(4\nu_T\tau))\,\mathrm{d}r, \tag{3.17}$$

$$\iint_S -\frac{c_f}{h}|\boldsymbol{v}|\omega\,\mathrm{d}S = \int_0^b -c_f\frac{\Gamma|\Gamma|}{8\pi h\nu_T\tau}[\exp(-r^2/(4\nu_T\tau)) - \exp(-r^2/(2\nu_T\tau))]\,\mathrm{d}r. \tag{3.18}$$

Moving with the vortex and taking h, ν_T and c_f to be approximately constant with r inside each vortex core, (3.17) and (3.18) can be evaluated using (2.9) and giving the following expressions:

$$\iint_S -\nu_T \frac{(\nabla\omega)^2}{\omega}\mathrm{d}S = -0.1321\frac{\Gamma}{\tau}, \tag{3.19}$$

$$\iint_S -\frac{c_f}{h}|\boldsymbol{v}|\omega \, \mathrm{d}S = -0.0372 \, \frac{c_f \, \Gamma|\Gamma|}{\pi \sqrt{\nu_T \, \tau} \, h}. \tag{3.20}$$

The dependence on the eddy viscosity ν_T and on the friction factor c_f appear only in (3.20), moreover h can only influence the bottom friction term. The latter means that moving in deeper waters, the bottom friction contribution decreases as $1/h$, hence reducing in intensity. Substituting (3.19) and (3.20) into (3.10) we obtain the total circulation reduction experienced by each vortex during its motion:

$$\frac{\mathrm{D}\Gamma}{\mathrm{D}t} = -\left(\frac{0.1321\pi\nu_T h + 0.0372 c_f |\Gamma| \sqrt{\nu_T \tau}}{\pi \nu_T h}\right) \frac{\Gamma}{\tau}. \tag{3.21}$$

Although (3.21) seems to suggests that the dissipation $\mathrm{D}\Gamma/\mathrm{D}t$ decreases with increasing eddy viscosity ν_T, the implicit dependence of Γ through the vortex size $b = 2\sqrt{\nu_T \tau}$ effectively leads to an increasing decay rate for an increasing ν_T.

4. The generation of circulation for the point vortices

To model the vorticity generation due to each breaking event over the bar and also at the shore, a simple equation is used, once the position where breaking occurs (see the simplified spatial model of Kennedy *et al.* 2006) and the offshore characteristics of the wave have been given, to compute the initial amount of circulation generated for each point vortex.

An analytical approach, valid for inhomogeneous wavetrains, to model the effects of a sloping beach on the nonlinear evolution of the vortical structures was used by BJ. They analysed the wave–mean flow interaction in the surf zone with a simple shallow-water model through an asymptotic expansion in the wave amplitude. In particular, it was possible to identify, by a careful scaling, both the early stages of vorticity growth and the later stages of vortex advection and decay due to bottom friction. To investigate and determine the intensity of circulation, Γ_{in}, of each point vortex at its generation, we focus our analysis on the early stages of motion, i.e. when vorticity is generated. The identification of the vorticity generation terms (due to wave breaking) becomes easier by using a Lagrangian approach, such as the GLM theory (Andrews & McIntyre 1978). At the considered initial stage, the effects of bottom friction can be neglected, while, since we are interested in the vortex generation, only the contributions of the dissipative force $\boldsymbol{F}$, due to breaking are retained. Introducing, in the GLM framework, a disturbance displacement $\xi(\boldsymbol{x}, t)$ and considering $\boldsymbol{F}'$ as the disturbance contribution to $\boldsymbol{F}$, we define $\mathscr{F}$ as:

$$\mathscr{F}_i = -\overline{\xi_{j,i} F'_j}, \tag{4.1}$$

where the overbar indicates GLM averaging.

Following BJ, for a steady wavetrain propagating in shallow waters with uniform frequency and a slowing-varying wavenumber vector field $\boldsymbol{k} = (k, l)$, for the generic ith component, the momentum equation becomes:

$$\frac{\mathrm{D}v_i}{\mathrm{D}t} + g\frac{\partial \overline{\Delta h}}{\partial x_i} = -\frac{1}{2}\frac{\overline{\partial |\boldsymbol{v}'|^2}}{\partial x_i} - \mathscr{F}_i, \tag{4.2}$$

where $\overline{\Delta h}$ is the water mean elevation, $\boldsymbol{v}'$ is the fluctuating velocity, both the Stokes drift $\boldsymbol{v}^S$ and the pseudomomentum $\boldsymbol{p}$ disappear because the assumptions made lead to constant $\boldsymbol{v}^S$ and $\boldsymbol{p}$, and the dissipative body force $\mathscr{F}$ is taken as significant only when waves break and is written in terms of the specific kinematic wave energy per

unit of surface area ($E \equiv gH^2/8$) as:

$$\mathscr{F} = \frac{\boldsymbol{k}}{h}\nabla \cdot \left(\frac{\boldsymbol{k}}{\kappa^2}E\right), \tag{4.3}$$

with $\kappa = |\boldsymbol{k}|$. Substituting (4.2) into (3.7) and again applying the Stokes' theorem, we obtain the following circulation equation, useful for evaluating the intensity of each point vortex at its generation:

$$\frac{\mathrm{D}\Gamma}{\mathrm{D}t} = -\iint_S (\nabla \times \mathscr{F}) \cdot \hat{\boldsymbol{k}}\, \mathrm{d}S. \tag{4.4}$$

Because of the assumption of uniform frequency and being in shallow water $c = \sqrt{g\,h}$, it is $\omega = \omega_0 = \kappa_0\sqrt{g\,h_0}$ which can be re-written as:

$$h\kappa^2 = h_0\kappa_0^2, \tag{4.5}$$

and where ω_0, κ_0 and h_0 are all quantities evaluated at the offshore location $\boldsymbol{x} = \boldsymbol{x}_0$.

Some approximations can be used to analyse (4.3). We assume a small-angle approximation for which the angle of incidence of waves to the beach is small, this means $|l_0| \ll \kappa_0$. Moreover, we assume that parallel rays originate at an offshore location with uniform wavenumber $\boldsymbol{k}(x_0, y) = (k_0, l_0)$ where k_0 and l_0 are constants.

Since the water depth is a function of both x and y, we should expect that not only can the wavenumber k change, but also l. To understand its physical meaning better and also to evaluate the right-hand side of (4.4), we can imagine being at the centre of the vortex and applying an appropriate rigid rotation on the reference frame, to obtain a wavenumber vector with one single component $\tilde{k}$, passing, therefore, from (x, y, z) to $(\tilde{x}, \tilde{y}, z)$. In this new reference frame, $\tilde{x}$ is parallel to the direction of wave propagation. In the $(\tilde{x}, \tilde{y}, z)$ frame, the curl of the dissipative body force $(-\nabla \times \mathscr{F})$, because of the assumptions made, simplifies to:

$$-\nabla \times \mathscr{F} = \mathscr{F}_{\tilde{x},\tilde{y}}, \tag{4.6}$$

while the expression for $\tilde{k}$ in the reference frame where $\tilde{l} = 0$ is obtained by means of (4.5):

$$\tilde{k} \approx \kappa = \kappa_0\sqrt{\frac{h_0}{h}}. \tag{4.7}$$

Equation (4.6) can be written in the following explicit form using (4.3) and (4.7):

$$\mathscr{F}_{\tilde{x},\tilde{y}} = \frac{\partial}{\partial\tilde{y}}\left\{\frac{\tilde{k}}{h}\frac{\partial}{\partial\tilde{x}}\left(\frac{E}{\tilde{k}}\right)\right\} = \frac{\partial}{\partial\tilde{y}}\left\{\frac{\partial}{\partial\tilde{x}}\left(\frac{E}{h}\right) + \frac{3}{2h}\frac{E}{h}\frac{\partial h}{\partial\tilde{x}}\right\}. \tag{4.8}$$

From Kelvin's theorem, circulation cannot be generated in the absence of the wave-breaking events. In the case of wave breaking, (4.8) clearly shows how a differential breaking caused by a non-uniform topography and the related energy gradient, can generate vorticity. In particular, the right-hand side of (4.8) can be regarded simply as a gradient in the direction normal to that of wave propagation, and therefore of breaking, of a quantity depending on both the wave energy and the local topography. From these considerations, it becomes evident that the radius b_0 of the core vortex should be chosen proportional to these gradients in the direction parallel to breaking. Equation (4.8) can be reduced in the analogous form derived in BJ by using the additional approximation $h = h(x)$.

We now integrate (4.8) over the vortex surface S centred at each point vortex and lying on a curve C circling the vortex and crossing the wave breaking event only

once. Γ is taken as positive if the integral over the closed material line C is taken in the clockwise direction. Retaining only the most significant contributions, we obtain the following form for the rate of circulation generation:

$$\frac{\mathrm{D}\Gamma}{\mathrm{D}t} \simeq -\int_1^2 \mathscr{F}_{\tilde{x}}\,\mathrm{d}\tilde{x} = -\int_1^2 \left[\frac{\partial \mathscr{E}}{\partial \tilde{x}} + \frac{3\mathscr{E}}{2h}\frac{\partial h}{\partial \tilde{x}}\right]\mathrm{d}\tilde{x}, \tag{4.9}$$

where E/h, the wave energy per unit of mass, is replaced by $\mathscr{E}$, while 1 and 2, in a bore-type approach, represent, respectively, two points placed seaward and shoreward of the breaking wave. Note that in the absence of dissipation, it is $\mathscr{F}=0$ along the $\tilde{x}$-direction, and (4.9), suggests conservation of $Eh^{1/2}=\mathscr{E}h^{3/2}$, as also reported in BJ.

Because of the previous assumptions and trying to simplify (4.9), we consider separately the generation of the bar and shore vortices. The former are, usually, generated when waves, approaching the beach, break on a bar (or a breakwater), whereas the latter are due to waves which break inshore of the bars/breakwater. For the bar vortices, consider waves starting to break over the bar slope at water depth h_B and continuing also over the bar crest. In the shallow-water framework, for shore-normal waves, the depth at which breaking starts (see Dean & Dalrymple 1984) is:

$$h_B = \left(H_0^2 C_{g0}\right)^{2/5}\gamma^{-4/5}g^{-1/5}, \tag{4.10}$$

where H_0 and C_{g0} are, respectively, the wave height and the group velocity at a given deep-water location. The parameter γ represents the ratio H_1/h for which waves break and it is, usually, taken as 0.78. Breaking is supposed to stop over the bar crest where the water depth h_c gives the depth-limited wave height $H_2=\beta h_c$, β being a parameter which, usually, assumes values around 0.45. With these assumptions, integral (4.9) gives:

$$\frac{\mathrm{D}\Gamma}{\mathrm{D}t} = \frac{5g\gamma^2}{16}(h_B - h_c) + \frac{gh_c}{8}(\gamma^2 - \beta^2), \tag{4.11}$$

which is the same expression as found by Brocchini *et al.* (2004) in the Eulerian framework.

We can perform a similar analysis for the generation of shore vortices, by observing that in the middle of the rip channel, waves break over a water depth h_B. Hence, in the rip channel, differential breaking occurs between h_B and h_s at which the waves, broken over the bar crests and reformed inshore of the bar, break a second time, because of the strong shoaling (see also figure 2). The water depth h_s is evaluated using (4.10) with reference to the wave height H_{0t} and to the group velocity C_{g0t} computed at the bar trough location (figure 2). To solve (4.9), we approximate $\hat{\mathscr{E}} \equiv (\mathscr{E}_1 + \mathscr{E}_2)/2$, to obtain:

$$\frac{\mathrm{D}\Gamma}{\mathrm{D}t} \simeq [\mathscr{E}_1 - \mathscr{E}_2] + \tfrac{3}{2}\hat{\mathscr{E}}\ln\left(\frac{h_1}{h_2}\right) = \frac{g}{8}\left(\gamma^2 h_B - \beta^2 h_s\right) + \frac{3g}{32}\left(\gamma^2 h_B + \beta^2 h_s\right)\ln\left(\frac{h_B}{h_s}\right), \tag{4.12}$$

which is a novel result, valid only for shore vortices.

5. Circulation dynamics on a rip-current bathymetry

In this section, we focus our attention on the flow dynamics obtained by using the PV approach and comparing it with two widely used wave-resolving and wave-averaged models. The chosen wave-averaged model is SHORECIRC, developed at

the University of Delaware it provides useful solutions for several coastal circulation systems (e.g. Putrevu & Svendsen 1999). The model uses the following depth-integrated and short-wave-averaged continuity and momentum equations:

$$\bar{\zeta}_{,t} + \nabla \cdot (h\tilde{\boldsymbol{v}}) = 0,$$
$$\tilde{\boldsymbol{v}}_{,t} + (\tilde{\boldsymbol{v}} \cdot \nabla)\tilde{\boldsymbol{v}} = -g\nabla\bar{\zeta} - \frac{1}{\rho h}\nabla \cdot (\boldsymbol{S} - \boldsymbol{T} + \boldsymbol{L}) - \frac{1}{\rho h}\boldsymbol{\tau}^B, \tag{5.1}$$

where $\bar{\zeta}$ is the mean surface elevation, h is the still-water depth, $\tilde{\boldsymbol{v}}$ is the depth-uniform velocity, $\boldsymbol{S}$ is the short-wave induced radiation stress (determined by a wave driver based on a parabolic mild slope equation, i.e. REF/DIF (see Kirby & Dalrymple 1994, for more details), $\boldsymbol{L}$ is the contribution from the depth-varying currents (the quasi-three-dimensional dispersive term), $\boldsymbol{T}$ is the depth-integrated turbulent shear stress tensor and $\boldsymbol{\tau}^B$ is the bottom friction term.

The set of Boussinesq-type equations used in the wave-resolving model FUNWAVE2D, developed at the University of Delaware (e.g. Wei *et al.* 1995) can correctly describe the fundamental features of the nearshore circulation, as shown in Chen *et al.* (1999). In particular, the continuity and momentum equations used in such a model are:

$$\eta_{,t} + \nabla \cdot \boldsymbol{M} = 0,$$
$$\boldsymbol{v}_{\alpha,t} + (\boldsymbol{v}_{\boldsymbol{\alpha}} \cdot \nabla)\boldsymbol{v}_{\boldsymbol{\alpha}} + g\nabla\eta + \boldsymbol{V}_1 + \boldsymbol{V}_2 = \boldsymbol{R}, \tag{5.2}$$

where $\boldsymbol{v}_\alpha$ is the reference two-dimensional velocity at a given elevation ($z = z_\alpha = -0.531\,h$, Chen *et al.* 2003), η is the free-surface elevation, $\boldsymbol{R}$ represents all dissipative forces and $\boldsymbol{M}$, $\boldsymbol{V}_1$ and $\boldsymbol{V}_2$ are the dispersive Boussinesq terms (see Chen *et al.* 2003 for more details).

The latter model provides an instantaneous description of coastal flows whose solutions are compared with the wave-averaged ones by applying a moving average over two short-wave periods. The two models predict different vorticity dynamics even if run with the same wave and topography configuration. In particular during the early stages, the vortical structures evolve slower in the wave-averaged computations than in the wave-resolving solutions, becoming faster with time.

The early stage locations of the vortical structures provide the initial positions of release for each vortex in terms of h_{in}. Obviously, the value of h_{in} is obtained by identifying the area where the vortex is generated. We focus on the initial stages when the circulation intensity, Γ_{in}, is obtained integrating the velocity field around a close material curve passing once through the wave breaking, where the vortex is generated. The group velocities C_{g0} and C_{g0t}, required to evaluate Γ_{in} from (4.11) and (4.12), have been derived, by means of linear wave theory expressions, from the simulation run with the wave driver REF/DIF.

Using a fairly standard configuration for this type of test (e.g. Haller *et al.* 2002), regular waves are run with an offshore wave height $H_0 = 7\,\mathrm{cm}$ and period $T = 1\,\mathrm{s}$ on a 1:40 sloping beach. These represent prototype conditions well for a geometric Froude scaling of about 1:20. From the simulations, we derive the intensity of the vorticity induced by the non-uniform wave breaking over the bar/breakwaters in a typical rip-current bathymetry.

Three different rip-current systems with different rip-channel size and cross-shore distance of the shoals are analysed in the following. All of them are obtained by approximating the bar as a Gaussian curve on a planar beach with the same slope as above, whereas as was done by Peregrine & Bokhove (1998), the rip channel is added

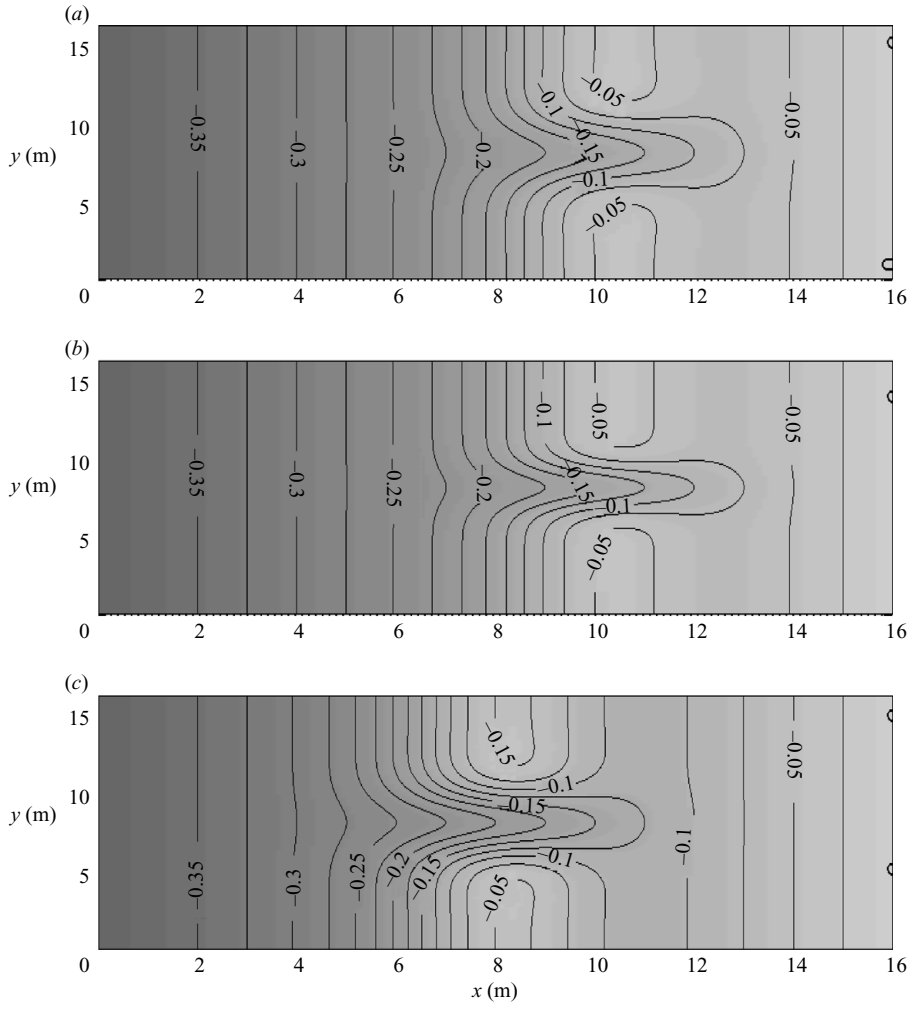

FIGURE 3. Rip bathymetries obtained from (5.3). Case (a): bathymetry obtained with $x_{ba} = 10\,\text{m}$, $M = 0.1$, $\sigma = 2$ and $a = 3$; case (b): bathymetry with a narrower rip-channel ($a = 2$); case (c): bathymetry with the bar moved offshore ($x_{ba} = 8\,\text{m}$), but with the same freeboard ($M = 0.15$ $\sigma = 2$ and $a = 3$).

through a function $f(y)$. Thus, the bed elevation is given by:

$$h = s(x - x_{sh}) + f(y)M \exp\{-[(x - x_{ba})/\sigma]^2\} \tag{5.3}$$

with

$$f(y) = 1 + \cos(2\pi y/L)[\exp(-(y - L/2)^2/a^2) + \exp(-(y - 3L/2)^2/a^2)], \tag{5.4}$$

in which s is the planar beach slope, x_{sh} is the value of x at the shoreline and it is equal to 16 m, being $x = 0\,\text{m}$ at the offshore boundary of the domain, x_{ba} is the crest bar position, M controls the bar height and σ and a the bar width, L is the maximum of the domain in the y-direction, equal to 18 m. Figure 3(a) shows the rip bathymetry obtained with $x_{ba} = 10\,\text{m}$, $M = 0.1$, $\sigma = 2$ and $a = 3$. In figure 3(b) the bathymetry is characterized by a narrower rip channel with $a = 2$ and in figure 3(c) the bar is moved offshore, but retains the same water depth over its crest with $x_{ba} = 8\,\text{m}$, $M = 0.15$,

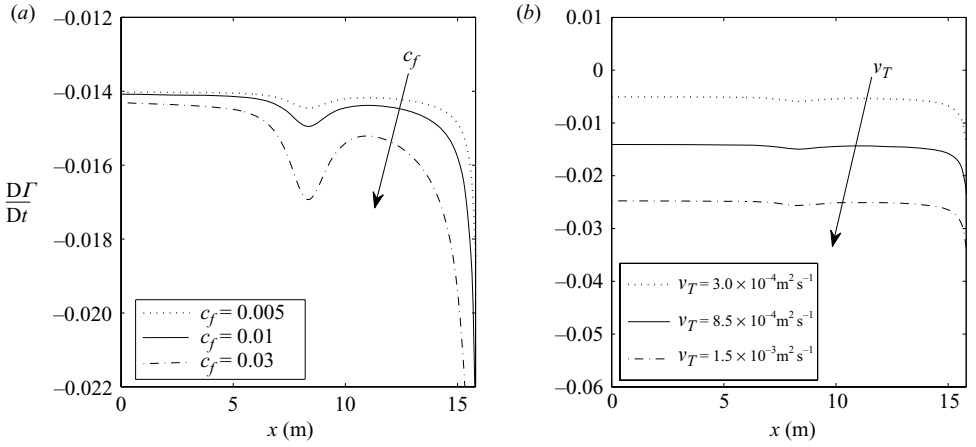

FIGURE 4. $D\Gamma/Dt$ evaluated for given vortex size in the case of the rip-current bathymetry (figure 3*a*). (*a*) Cross-shore profile of $D\Gamma/Dt$ for fixed eddy viscosity ($\nu_T = 8.5 \times 10^{-4}\,m^2\,s^{-1}$) and for different values of the friction factor. (*b*) Cross-shore profile of $D\Gamma/Dt$ for fixed friction factor ($c_f = 0.01$) and for different values of the eddy viscosity.

$\sigma = 2$ and $a = 3$. The latter bathymetry has been chosen with the aim of reducing the eventual differences in the modelling of the near-shoreline motion used in the various models.

We first focus on the bar vortices which arise from this rip bathymetry and obtain the initial data from the related numerical simulations. From such simulations, a typical value of eddy viscosity of $8.5 \times 10^{-4}\,m^2\,s^{-1}$ is chosen. Equation (3.21) does not have a trivial solution: on its right-hand side h, Γ and the decay time τ are time dependent through the vortex position. In the PV solver, the lifetime of each vortex τ is practically computed, following (2.7), as the ratio between the sum of the vortex radius evaluated at each time step and multiplied for the δt used, and the vortex radius at time t.

Keeping in mind that larger viscosities induce larger diffusion and, therefore, larger core vortex sizes b, see (2.9), we plot in figure 4 the dissipation rate for a given radius b. The results shown in this figure have been obtained with a fixed value of the circulation intensity $\Gamma_{in} \simeq 0.1047\,m^2\,s^{-1}$ found by using (4.11), valid in the case of bar vortices. We parametrically plot the quantity $D\Gamma/Dt$ for the case (*a*) bathymetry using different values for the friction factor, $0.005 < c_f < 0.030$ (figure 4*a*), and for the eddy viscosity, $3.0 \times 10^{-4}\,m^2\,s^{-1} < \nu_T < 1.5 \times 10^{-3}\,m^2\,s^{-1}$ (figure 4*b*). We observe that the growth of the friction factor corresponds to an increased dissipation of $D\Gamma/Dt$, and, as expected, the same happens by increasing the eddy viscosity ν_T. Similar results are obtained also for bathymetries in figures 3(*b*) and 3(*c*), but are not here reported for the sake of brevity.

From figure 4 it is evident that the rate of dissipation is small in the offshore area of the domain. Moving shorewards, i.e. for $x \geqslant 14.5\,m$, where self-advection velocities become more important because of the shallow waters, the vortex is subjected to a stronger dissipation. In particular, in all three cases, the effects of the bar presence induce a stronger local dissipation because of the shallower waters. Such stronger dissipation contributes to bound the shore vortices in between the shoreline and the bar, leaving them little chance to move offshore.

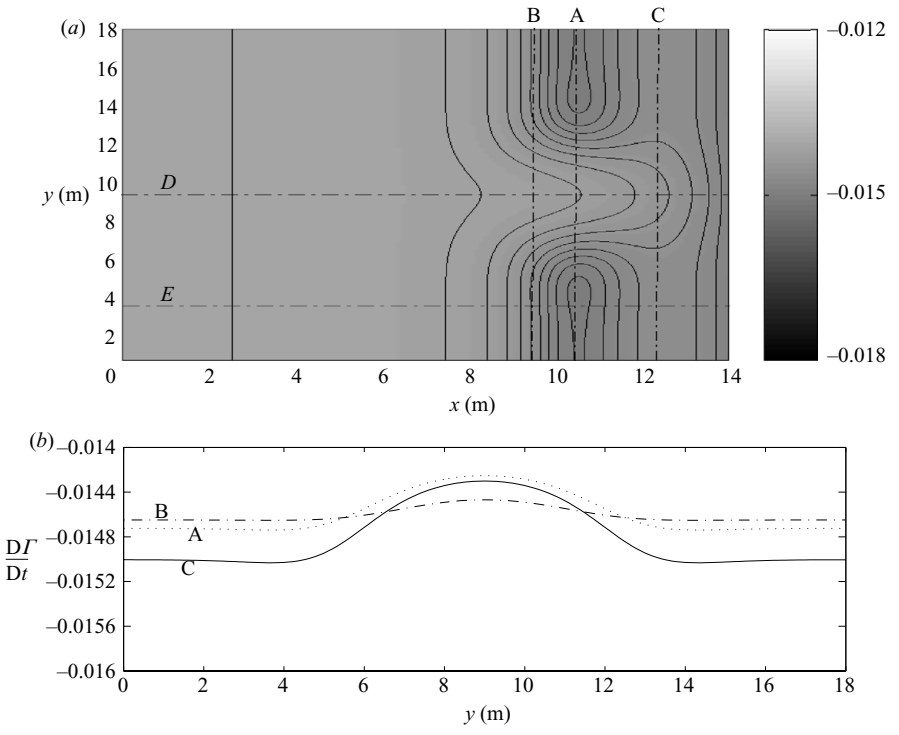

FIGURE 5. $D\Gamma/Dt$ of (3.21) evaluated for given vortex size in the case of the rip-current bathymetry (figure 3*a*) with $c_f = 0.01$ and $\nu_T = 8.5 \times 10^{-4}\,\mathrm{m^2\,s^{-1}}$: (*a*) the complete spatial distribution and (*b*) three longitudinal sections, over the bar crest A, (solid line), offshore from the bar B, (dash-dotted line), and shorewards of the bar C, (dotted line).

Finally, figure 5(*b*) shows the spatial distribution of $D\Gamma/Dt$ for the rip current bathymetry of case (*a*), from which it is clear that stronger dissipations of Γ occur over the bar crest and close to the shoreline. Longshore sections (A, B, C) at different values of x are analysed. Comparing the rate of change of Γ along such three sections, we pinpoint the region where the circulation dissipation has the largest influence on the vortex dynamics. The dash-dotted line refers to an offshore section (B in the figure), the solid line to a section over the bar crest (A in the figure) and the dotted line to a section in the bar trough (C in the figure). The rip channel reduces the dissipation of Γ, especially at the bar location.

In figure 6 we give the velocity and vorticity fields for the three models at some chosen time steps, t_1, t_2 and t_3. Because of the different velocity of the overall dynamics resulting from the three models, we choose to compare them at the same dynamical steps. This means comparing the models at instants with similar hydrodynamics main features. Single-point vortices are placed at the location where, from the numerical simulations, differential breaking occurs (both over the bar and near the shoreline), therefore, two bar vortices and two shore vortices are input at such location at each wave period. Vortices are removed from the domain once they reach the boundaries. Hence, once quasi-steady conditions are reached, an almost-constant number of vortices populate the domain. Since the near-shoreline differential breaking observed in our simulations is rather weak (see figure 2 for a qualitative inspection), the position where such vortices are generated is not well localized as, instead, it occurs

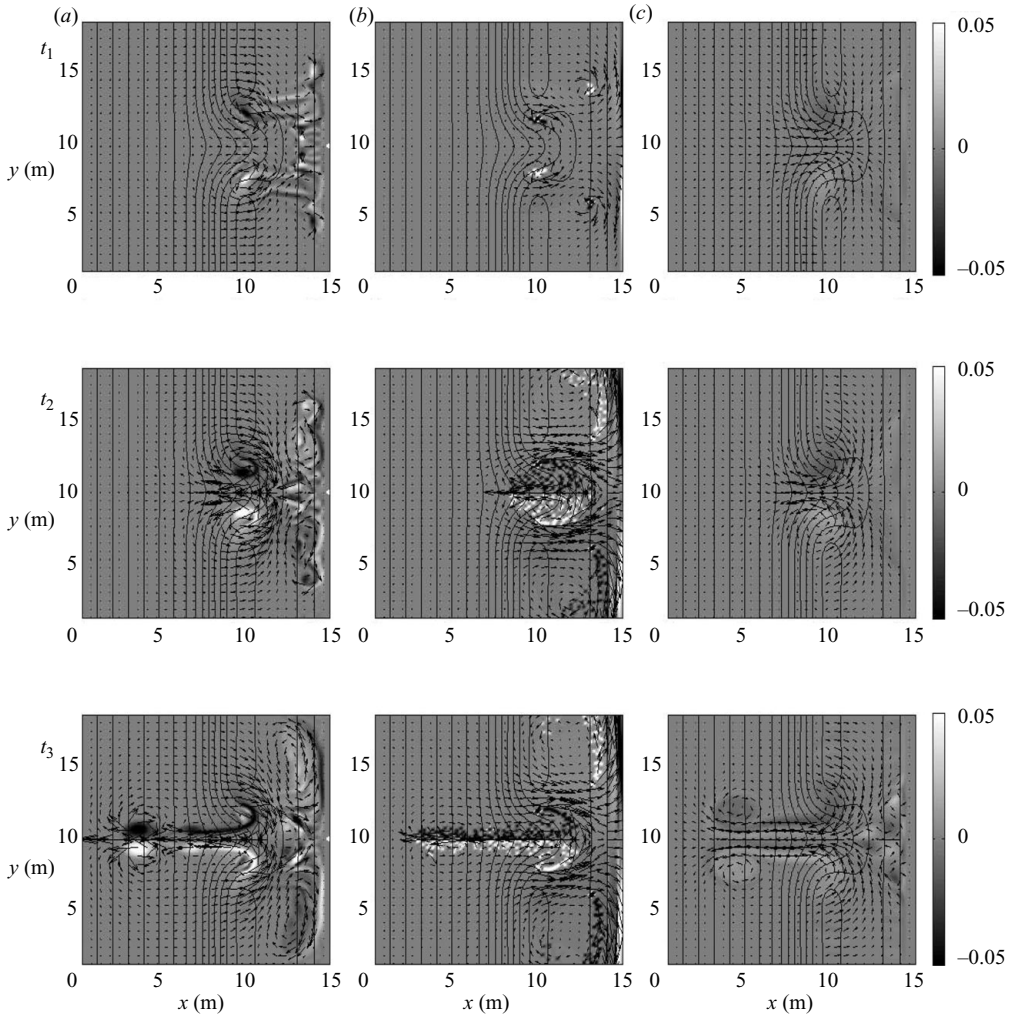

FIGURE 6. Velocity and vorticity fields predicted by (*a*) SHORECIRC, (*b*) PV model and (*c*) FUNWAVE2D at three different time steps t_1 (top panels), t_2 (middle panels) and t_3 (bottom panels) for bathymetry of figure 3(*a*).

for the bar vortices. Since in the PV model, vortex initial locations and intensities must be determined *a priori*, input of the shore macrovortices over a small area could represent a limit for the PV model. At any rate, use of the PV approach leads to good results also in the assessment of the shore macrovortices dynamics, in particular, during stages t_2 and t_3 (figure 6).

Inspection of figure 6 also reveals that with the chosen bathymetry (figure 3*a*) and offshore wave field, both numerical models, in particular the wave-resolving model, predict at the initial time t_1, generation of weak and wide shore vortices which, in view of the theoretical framework illustrated in §§ 2 and 4, are a clear illustration of a weak and spatially uniform breaking near the shoreline. However, note that the filtering operation, which is applied near the shoreline in the wave-resolving model FUNWAVE2D and related to its slot-type boundary condition, could be one of the reasons for weaker shore vortices generated by the mentioned model, compared to

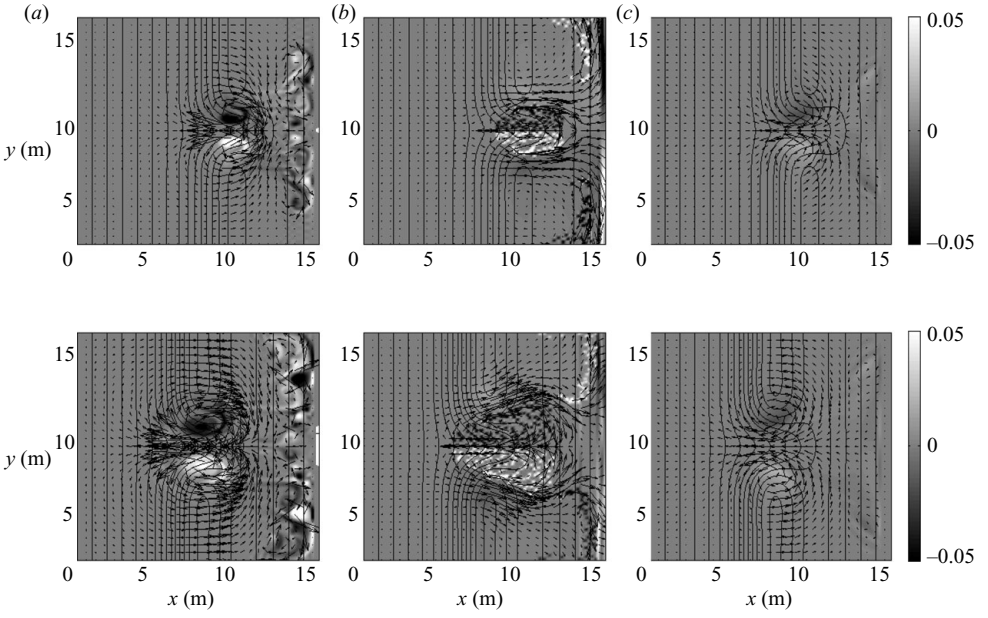

FIGURE 7. Velocity and vorticity fields predicted by the models under analysis for the stage t_2 flow. Top panels: bathymetry in figure 3(*b*). Bottom panel: bathymetry in figure 3(*c*). For graphical arrangements see figure 6.

the wave-averaged and the PV models. The flow patterns obtained with bathymetries in figures 3(*b*) and 3(*c*) are qualitatively very similar to those obtained the case in figure 3(*a*).

This can be easily observed from figure 7 in which, with graphical arrangements similar to those of figure 6, velocity and vorticity fields of the stage flow t_2 are reported for bathymetries in figures 3(*b*) and 3(*c*). A reduction in the dimensions of the rip-channel (figure 7, top panels), gives stronger shore vortices, this is particularly evident from the wave-averaged solution, while the bar macrovortices decrease their size in all solutions. In this case for the PV model we also observe that, because of the larger slope characterizing the rip-channel, single-point vortices are influenced by stronger self-advection velocities and, therefore, immediately after their generation, move faster shoreward. An increase in the distance of the shoal from the shore (figure 7, bottom panels), leads to wider bar macrovortices, not only in the PV solutions, but also in the wave-averaged and wave-resolving solutions. Moreover, weaker shore macrovortices are predicted by both the wave-averaged and the wave-resolving models.

The initial time step t_1, corresponding to *stage 1* of Brocchini *et al.* (2004), occurs, approximately, for all models at $t \simeq 15\,\mathrm{s}$ when both bar vortices and shore vortices are generated and the point vortices start to roll up in macrovortices. In particular, we observe that the wave-resolving model predicts weak shore vortices while the wave-averaged and, of course, the PV model predict well-defined shore vortices.

The following two steps t_2 and t_3 are much more interesting and are defined as the early stage and the later stage of evolution, respectively. Figure 8 reports cross-shore velocities at the two steps t_2 and t_3 for the mid rip-channel section D of the case (*a*) bathymetry of figure 3(*a*) (see figure 5).

The early stage, t_2, corresponds to *stage 2* described by Brocchini *et al.* (2004). At this stage, vortex motions are characterized by strong self-advection velocities due to

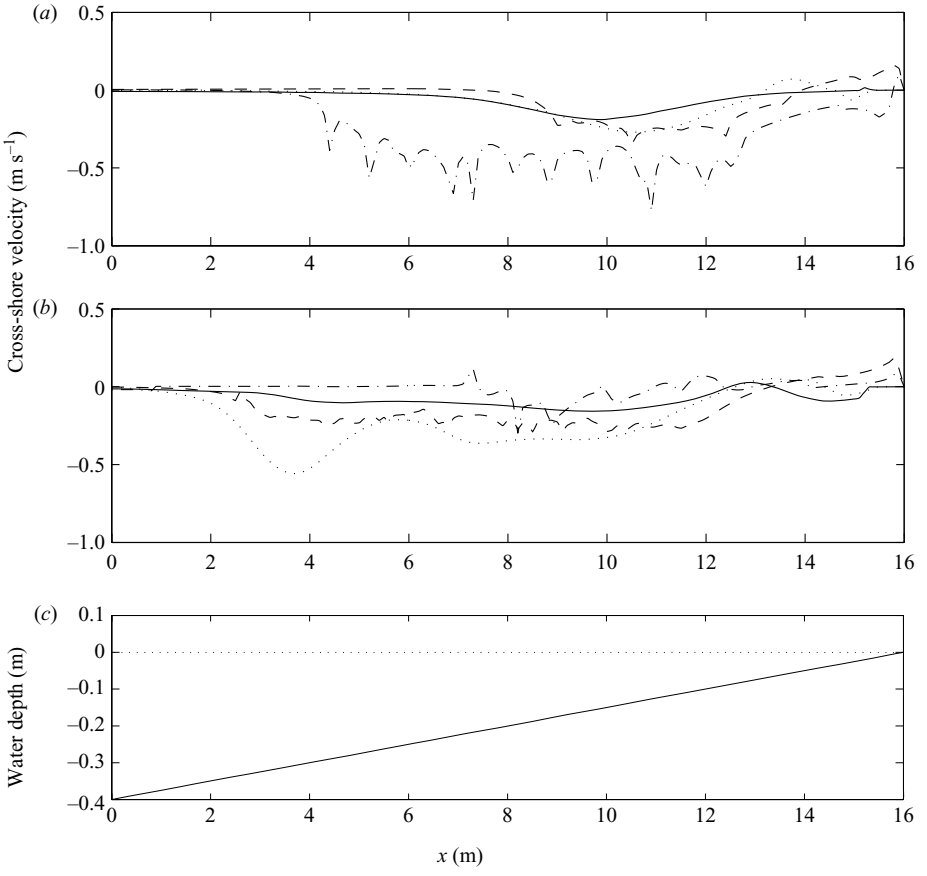

FIGURE 8. Cross-shore velocity computed at the cross-shore section D of figure 5 of the rip channel. Results from a wave-averaged simulation run with SHORECIRC (dotted line), from a wave-resolving simulation run with FUNWAVE2D (solid line) and from the dissipative PV model (dashed line) and from the inviscid PV model (dash-dotted line), are plotted for (*a*) steps t_2 and (*b*) t_3 of evolution. (*c*) For reference, the bathymetry of the chosen section D.

the bottom slope and weak mutual-advection effects. Moreover, the shore vortices just formed move slowly in the longshore direction and the bar vortices move, following the isobaths, towards the centre of the rip channel, becoming closer together.

The later stage, t_3, as described by Brocchini *et al.* (2004) in their *stage 3*, is characterized by an increasing mutual interaction between the bar macrovortices, being closer to each other, and weaker self-advection velocities, being in deeper water. The two bar macrovortices slowly move offshore outside the rip channel where they have been generated, while the two shore macrovortices move in the alongshore direction.

When evaluating the results of figure 8 and subsequent ones, it should be borne in mind that the PV model neglects some important processes such as the wave–mean flow interaction, gravity waves, instabilities and background currents. The dash-dotted line represents the results from the PV model run without the dissipative contributions studied in § 3. The flow dynamics in the rip channel predicted by the PV model seem to be of the same order of magnitude as the other two numerical solutions.

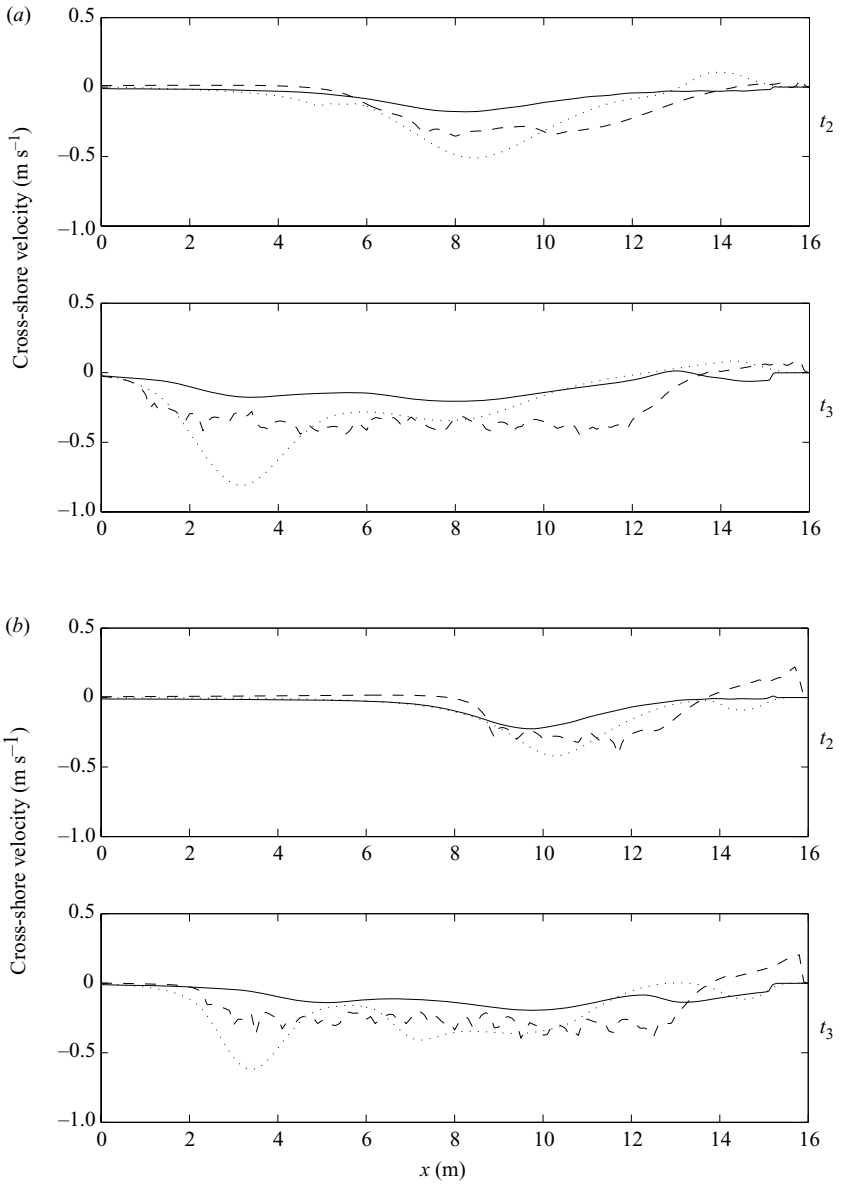

FIGURE 9. Cross-shore velocity computed at the cross-shore section of the rip channel (section D) for (*a*) bathymetry of figure 3(*b*) and (*b*) of figure 3(*c*). Results from a wave-averaged simulation run with SHORECIRC (dotted line), from a wave-resolving simulation run with FUNWAVE2D (solid line) and from the dissipative PV model (dashed line), are plotted for the steps t_2 and t_3 of the evolution.

Analysis of the cross-shore velocity at chosen sections reveals that absence of dissipative mechanisms in the PV approach (dash-dotted line in figure 8) leads to rather different results from those given by both the wave-resolving and the wave-averaged model. In more detail, the rip current predicted by an inviscid PV model, without the dissipative contributions studied in § 3, is initially stronger (see figure 8*a*) and leads to a late-stage flow characterized by no coherent structures. The absence of viscous effects and the consequent absence of well-organized macrovortices leads, at

	Case (*a*)		Case (*b*)		Case (*c*)	
	PV-WA	PV-WR	PV-WA	PV-WR	PV-WA	PV-WR
t_2	0.6	0.5	0.7	0.5	0.6	0.5
t_3	0.7	0.3	0.7	0.5	0.7	0.6

TABLE 1. Correlation coefficients between the PV model and both the wave-averaging (WA) and wave-resolving (WR) models.

any times, to the spiky rip-current profile shown by the dash-dotted line of figure 8. A main difference with the dissipative PV model is in the stronger mutual-interactions among the point vortices and more intense self-advection velocities which make, as also described in Kennedy (2003), the point vortices migrate rapidly away from the input position. Such rapid evolution does not give point vortices enough time to roll up into macrovortices and generate well-defined coherent structures. Finally, single-point vortices are more spread than in the dissipative case, hence, the spiky velocity distributions of figure 8 (dash-dotted line) reflecting the contributions of isolated point vortices.

Figure 9 shows the cross-shore velocities computed in the rip-channel section for bathymetries of figures 3(*a*) and 3(*b*), at the chosen two steps of evolution. Also for the bathymetric conditions, the dissipative PV model can reproduce rip-current velocities fairly well, not only in the rip-neck, as shown by Kennedy (2003) by means of the inviscid model, but also in the region offshore from the bar. A quantitative comparison between the PV model results and those achieved by means of both the wave-averaged and the wave-resolving models is obtained by computing the correlation coefficients for the rip current. In table 1, these coefficient are reported for the results obtained for all bathymetries at times t_2 and t_3. These results show that, in reflection of the common nature of the two models which do not explicitly compute wave propagation, a better agreement is found between the PV and the wave-averaged model.

Moreover in figure 10, the alongshore velocity component is plotted along section E (see figure 5) for all bathymetries (*a*), (*b*) and (*c*). Differences between the wave-resolving (solid line) and the wave-averaged (dotted line) solutions emerge independently of the bathymetry used. Because of the more intense shore vortices, SHORECIRC predicts, close to the shoreline, higher negative longshore velocities, matching fairly well the results given by the PV model (dashed line). The wave-resolving model provides, as discussed above, at the same cross-shore section and for both stages t_2 and t_3, weaker positive longshore velocities.

6. Conclusions

The dissipative PV model described in this paper is based on a generation-of-vorticity approach, where oppositely signed vortices are continuously released in the most appropriate generation area and set free in the system. Inclusion of dissipative contributions largely improves the flow representation of the analogous inviscid model, in principle similar to that of Kennedy (2003), whose solutions compare poorly with solutions of widely used wave-averaged (SHORECIRC) and wave-resolving (FUNWAVE2D) numerical models, and provides a fairly good general description of the nearshore circulation induced over rip-current bathymetries.

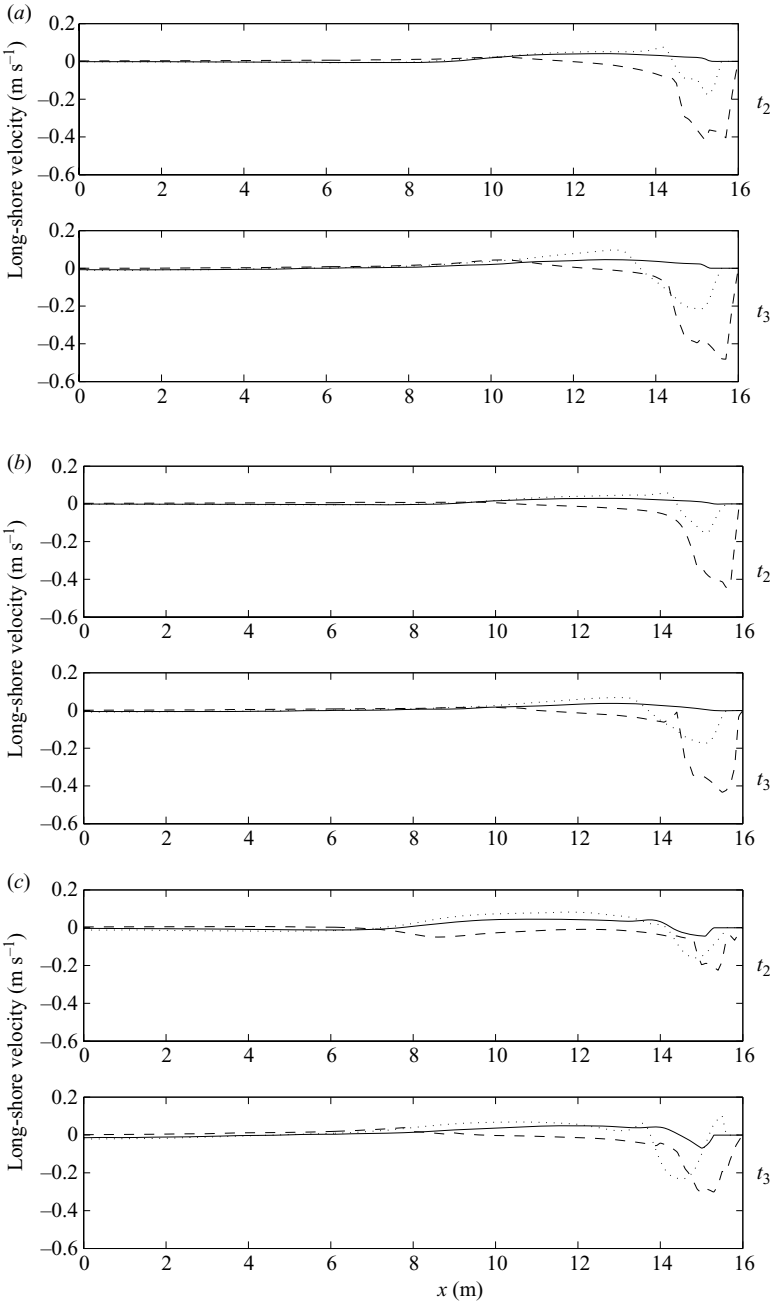

FIGURE 10. Longshore velocity computed at the cross-shore section E outside the rip channel of figure 5. (*a*) Case (*a*), (*b*) case (*b*), (*c*) case (*c*). Results from a wave-averaged simulation run with SHORECIRC (dotted line), from a wave-resolving simulation run with FUNWAVE2D (solid line) and from the viscous PV model (dashed line), are plotted together at steps t_2 and t_3 of evolution.

The vorticity sources, used in this model, are those due to the wave breaking. Once the location where point vortices are generated and the offshore wave field have been chosen, the model provides, at a reduced computational cost (the time required to

run the PV model is approximately the same as that needed for the wave-averaged model and about one order of magnitude less than that needed by the wave-resolving model), a simplified description of the nearshore circulation. The flow description includes the influence of a complex topography (affecting the self-advection velocity of the vortex), the bottom friction and viscous effects acting on each point vortex. The generation and dissipation of the point vortices have been studied and analytical relationships have been obtained with the water depth of wave breaking (generation) and of vortex migration (dissipation).

Results have been obtained using three 'typical' rip-current bathymetries for which we also test the model comparing the vorticity dynamics with the results obtained with both wave-resolved and wave-averaged numerical solutions. A comparison of dynamically equivalent flow configurations shows that the dissipative PV model solutions, neglecting any influence of the wave field, provides rip current velocities in good agreement with both numerical models. In particular, the correlation coefficients for the rip-current solution have been computed to quantify the comparison between the PV model and both the wave-averaged and wave-resolving models. In reflection of the common nature of the two models which do not explictly compute wave propagation, a better agreement is found between the PV and the wave-averaged model. Obviously, the PV model performs best for flows and regions strongly affected by vortical structures.

This work is part of the PhD thesis of Emanuele Terrile to be submitted in partial fulfilment of his degree. The financial support of the Italian MIUR through the grant INTERLINK-II04C02L8E is acknowledged.

REFERENCES

Andrews, D. G. & McIntyre, M. E. 1978 An exact theory of nonlinear waves on a Lagrangianmean flow. *J. Fluid Mech.* **89**, 609–646.

Brocchini, M. & Colombini, M. 2004 A note on the decay of vorticity in shallow flow calculations. *Phys. Fluids* **16**, 2469–2475.

Brocchini, M., Kennedy, A. B., Soldini, L. & Mancinelli, A. 2004 Topographically controlled, breaking-wave-induced macrovortices. Part 1. Widely separated breakwaters. *J. Fluid Mech.* **507**, 289–307.

Bühler, O. 2000 On the vorticity transport due to dissipating or breaking waves in shallow-water flow. *J. Fluid Mech.* **407**, 235–263.

Bühler, O. & Jacobson, T. E. 2001 Wave-driven currents and vortex dynamics on barred beaches. *J. Fluid Mech.* **449**, 313–339.

Centurioni, L. R. 2002 Dynamics of vortices on a uniformly shelving beach. *J. Fluid Mech.* **472**, 211–228.

Chen, Q., Kirby, J., Dalrymple, R., Kennedy, A. B. & Haller, M. 1999 Boussinesq modelling of a rip current system. *J. Geophys. Res. Oceans* **104**, 20 617–20 637.

Chen, Q., Kirby, J., Dalrymple, R., Shi, F. & Thornton, E. B. 2003 Boussinesq modeling of longshore currents. *J. Geophys. Res.* **108** (C11), 3362.

Dean, R. G. & Dalrymple, R. 1984 *Water Wave Mechanics for Engineers and Scientists*. Prentice-Hall.

Haller, M. C., Dalrymple, R. A. & Svendsen, I. A. 2002 Experimental study of nearshore dynamics on a barred beach with rip channels. *J. Geophys. Res. Oceans* **107**(C6), 3061.

Kennedy, A. B. 2003 A circulation description of a rip current neck. *J. Fluid Mech.* **497**, 225–234.

Kennedy, A. B., Brocchini, M., Soldini, L. & Gutierrez, E. 2006 Topographically controlled, breaking-wave-induced macrovortices. Part 2. Changing geometries. *J. Fluid Mech.* **559**, 57–80.

Kennedy, A. B. & Thomas, D. A. 2004 Drifter measurements in a laboratory rip current. *J. Geophys. Res. Oceans* **109**(C8), doi:10.1029/2003JC001982.

Kirby, J. T. & Dalrymple, R. A. 1994 REF/DIF, Version 2.5 *Cent. for Appl. Coastal Res. Univ. of Delaware, Internal Rep. CACR-94-22.* Newark, Delaware.

Lamb, H. 1932 *Hydrodynamics.* Dover.

Peregrine, D. H. 1998 Surf zone currents. *Theor. Comput. Fluid Dyn.* **10**, 295–309.

Peregrine, D. H. 1999 Large-scale vorticity generation by breakers in shallow and deep water. *Eur. J. Mech.* B/*Fluids***18**, 403–408.

Peregrine, D. H. & Bokhove, O. 1998 Vorticity and surf zone currents. *Proc. 26th Intl Conf. Coastal Engng ASCE* Copenhagen vol. 1, pp. 745–758.

Piattella, A., Brocchini, M. & Mancinelli, A. 2006 Topographically controlled, breaking-wave-induced macrovortices. Part 3. The mixing features. *J. Fluid Mech.* **559**, 81–106.

Putrevu, U. & Svendsen, I. A. 1999 Three-dimensional dispersion of momentum in wave-induced nearshore circulation. *Eur. J. Mech.* B/*Fluids* **18**, 409–427.

Saffman, P. G. 1970 Velocity of viscous vortex ring. *Stud. Appl. Maths* **49**, 371.

Terrile, E., Briganti, R., Brocchini, M. & Kirby, J. 2006 Topographically-induced enstrophy production/dissipation in coastal models. *Phys. Fluids* **18** (12), 126603.

Tung, C. & Ting, L. 1967 Motion and decay of a vortex ring. *Phys. Fluids* **10**, 901–910.

Wei, G., Kirby, J., Grilli, S. T. & Subramanya, R. 1995 A fully nonliner Boussinesq model for surface waves. Part 1. Highly nonlinear, unsteady waves. *J. Fluid Mech.* **294**, 71–92.